J. Fluid Mech. (2005), *vol.* 523, *pp.* 339–365.
DOI: 10.1017/S0022112004002149 Printed in the United Kingdom

The need for a pressure-term representation in empirical Galerkin models of incompressible shear flows

By BERND R. NOACK[1]†, PAUL PAPAS[2]‡ AND PETER A. MONKEWITZ[2]

[1]Hermann-Föttinger-Institut für Strömungsmechanik, Technische Universität Berlin HF1, Straße des 17. Juni 135, D-10623 Berlin, Germany

[2]Fluid Mechanics Laboratory (LMF), Swiss Federal Institute of Technology (EPFL), CH-1015 Lausanne, Switzerland

(Received 25 August 2003 and in revised form 3 August 2004)

Low-dimensional empirical Galerkin models are developed for spatially evolving laminar and transitional shear layers, based on a Karhunen–Loève decomposition of incompressible two- and three-dimensional Navier–Stokes simulations. It is shown that the key to an accurate Galerkin model is a novel analytical pressure-term representation. The effect of the pressure term is elucidated by a modal energy-flow analysis in a mixing layer, which generalizes the framework developed by Rempfer (1991). In convectively unstable shear layers, it is shown in particular that neglecting small energy terms leads to large amplitude errors in the Galerkin model. The effect of the pressure term and small neglected energy flows is very important for a two-dimensional mixing layer, is less pronounced for the three-dimensional analogue, and can be considered as small in an absolutely unstable wake flow.

1. Introduction

In this study, a low-dimensional empirical¶ Galerkin model of the laminar and transitional shear layer is proposed. The oncoming flow is represented by a tanh-profile, perturbed by a small, spatially growing eigenmode obtained from a local linear stability analysis. Since instabilities of tanh-profiles have been extremely well-studied this flow is ready for the current additional analysis. This study is motivated by the open questions still remaining in the area of low-dimensional models used in flow control applications.

In the past, low-dimensional modelling of coherent structures was primarily considered as a means for testing physical understanding. Examples include Townsend's (1956) rigorous analytical study of coherent structure dynamics in turbulence, Lorenz's (1963) celebrated three-mode model of Rayleigh–Bénard convection, and the 'Cornell model' (Aubry *et al.* 1988) of the turbulent boundary layer. The Cornell model has inspired many subsequent empirical Galerkin models with

† Author to whom correspondence should be addressed: Bernd.R.Noack@tu-berlin.de
‡ Present address: Division of Engineering, Colorado School of Mines, Golden, CO 80401, USA.
¶ The terminology of Rempfer (1991) is adopted in which Galerkin models based on a Karhunen–Loève decomposition are called 'empirical,' since their construction requires *a priori* knowledge from the full Navier–Stokes solution or from experiment.

Karhunen–Loève decompositions (see, for instance, Holmes, Lumley & Berkooz 1998). Meanwhile, many low-dimensional modelling efforts are targeting flow control applications for two main reasons. On the one hand, such 'plant models' allow the use of all the powerful tools of control theory and, on the other hand, quick exploratory actuation studies are made possible by the simplicity of the model.

A large number of flow control problems are strongly related to the manipulation of coherent structures in shear layers (Gad-el-Hak 1996, 2000). Engine-related examples include separation control of a diffuser (Coller *et al.* 2000), the control of high-frequency jet noise near the engine exhaust (Narayanan, Noack & Meiburg 2002), afterburner screech due to mixing processes in the shear layer from flame holders (Rogers & Marble 1954), and the enhancement of combustor mixing in a dead-water region (Noack *et al.* 2004*a*).

A first class of low-dimensional coherent-structure representations of shear-layer dynamics are the vortex models, which have not surprisingly proven to be particularly robust and successful (Coats 1997). Their success began with Rosenhead's (1930) first point-vortex simulation of the temporally growing two-dimensional shear layer and continues with Ashurst & Meiburg's (1988) pioneering vortex-filament computation. The inviscid nature of the Kelvin–Helmholtz instability and the Lagrangian vortex dynamics are ideal for the application of vortex methods. Some recent control strategies are based on confined vortex models of actuated flow and on efficient methods of nonlinear control theory (Noack *et al.* 2004*a*; Tadmor & Banaszuk 2002). However, the hybrid nature of open vortex models with continuous production, merging and elimination of vortices complicates the application of control theory methods (Pastoor *et al.* 2003).

Another class of models is formed by low-dimensional Galerkin models which, for the shear layer, appear to be more challenging to construct than corresponding vortex models. One reason for this challenge is the Galerkin ansatz itself, i.e. the superposition of a few (global) modes to represent the convective amplification of Kelvin–Helmholtz-type vorticity concentrations. For the turbulent jet and mixing layer, Karhunen–Loève decompositions (Delville *et al.* 1999) and Galerkin models (Rajaae, Karlsson & Sirovich 1994; Ukeiley *et al.* 2001) have been constructed from experimental data. Delville's group has pioneered the development of similar low-dimensional representations of turbulent mixing layers from large-eddy simulation data (Cordier, Tenaud & Delville 1998). These models require empirical assumptions, for instance an eddy-viscosity model to incorporate the effect of neglected turbulent fluctuations, the Cornell model for the base-flow variation, or periodicity in the streamwise direction to complete experimental data. In the category of absolutely unstable flows, a 10-dimensional Galerkin model has recently been developed by Wee *et al.* (2002) for a two-dimensional shear layer behind a backward-facing step at $Re = 5000$. The present study completes the spectrum of low-dimensional shear-layer models in the laminar and transitional regime in which no empirical input beyond the Karhunen–Loève modes is needed.

In control applications, actuation prediction with empirical Galerkin models is still in its infancy. Examples include the volume-force actuation for skin-friction reduction in a turbulent boundary layer by Blossey & Lumley (1998), another volume-force application for the suppression of vortex shedding by Gerhard *et al.* (2003), and a 4-mode model of an acoustic actuator by Rediniotis, Ko & Kurdila (2002).

In the present study, it is demonstrated how the accuracy of empirical Galerkin models for shear flows can be significantly improved by introducing an appropriate pressure-term representation. The manuscript is organized as follows: In § 2 a

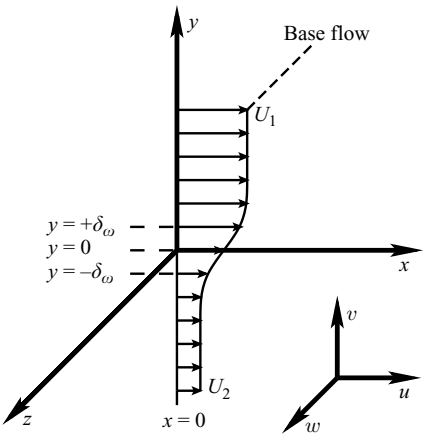

FIGURE 1. Coordinate system and velocity profile.

low-dimensional Galerkin model enhanced by a novel pressure-term representation is described. This model is then used to describe two-dimensional laminar Kelvin–Helmholtz vortices in § 3, and a transitional shear layer in § 4. The main findings and the potential implications for other flows are summarized in § 5.

2. Low-dimensional modelling

In this section, the low-dimensional modelling process from Navier–Stokes simulations to Galerkin models is described. In § 2.1, the flow configuration and Navier–Stokes solver are outlined. The local linear stability stability analysis in § 2.2 provides the unsteady inflow condition of the simulation. In § 2.3, a straightforward empirical Galerkin model is constructed from the simulation data and a new model for the pressure term is proposed in § 2.4. Finally, energy balance equations for each mode are derived in § 2.5.

2.1. *Navier–Stokes simulation of the spatially evolving shear layer*

The flow is described in a Cartesian coordinate system x, y, z, where the positive x-axis is aligned with the mean flow, the positive y-axis with the gradient of the streamwise velocity and the negative z-axis with the vorticity (see figure 1). The origin 0 of the coordinate system is in the centreplane of the upper and lower streams. Locations are defined by the vector $\boldsymbol{x} := (x, y, z)$, the unit vectors in the x-, y-, and z-directions are denoted by $\hat{\boldsymbol{e}}_x$, $\hat{\boldsymbol{e}}_y$ and $\hat{\boldsymbol{e}}_z$, respectively, and the corresponding components of the velocity vector $\boldsymbol{u}$ by u, v and w.

The shear layer is characterized by the (unperturbed) velocity U_1 of the fast upper stream, far away from the shear layer, the velocity U_2 of the slow lower stream, the vorticity thickness δ_v of the shear layer, and the kinematic viscosity ν of the fluid (Monkewitz & Huerre 1982). For convenience, the shear-layer thickness $\delta_\omega = \delta_v/2$ is introduced as reference scale for this study. The above parameters give rise to two independent non-dimensional control parameters: the Reynolds number

$$Re = \frac{U_1 \delta_\omega}{\nu} \tag{2.1}$$

and the velocity ratio

$$\gamma = \frac{U_1}{U_2}. \tag{2.2}$$

In the framework of linear stability theory, it is customary to use a modified velocity ratio, $\Gamma = (\gamma - 1)/(\gamma + 1)$, as in Monkewitz & Huerre (1982) for instance. Following Michalke (1964) and many others, a hyperbolic base profile is taken to represent the shear-layer profile, here at the inflow $x = 0$ of the computational box,

$$\boldsymbol{u} = U(y)\,\hat{\boldsymbol{e}}_x \quad \text{where} \quad U(y) = \frac{U_1 + U_2}{2} + \frac{U_1 - U_2}{2}\,\tanh\left(\frac{y}{\delta_\omega}\right). \tag{2.3}$$

In the following, all quantities are made non-dimensional with the maximum velocity U_1, the shear-layer thickness δ_ω, and the constant density of the fluid ρ.

The continuity equation

$$\nabla \cdot \boldsymbol{u} = 0 \tag{2.4}$$

and the Navier–Stokes equations

$$\partial_t \boldsymbol{u} + \nabla \cdot (\boldsymbol{u}\boldsymbol{u}) = -\nabla p + \frac{1}{Re}\Delta \boldsymbol{u} \tag{2.5}$$

are solved in a rectangular domain Ω of streamwise length L, transverse dimension H, and spanwise width W,

$$\Omega := \{(x, y, z) : 0 \leqslant x \leqslant L \quad \wedge \quad |y| \leqslant H/2 \quad \wedge \quad 0 \leqslant z \leqslant W\}. \tag{2.6}$$

In the spanwise direction, periodicity with wavelength W is assumed, i.e.

$$\boldsymbol{u}(\boldsymbol{x} + W\,\hat{\boldsymbol{e}}_z, t) = \boldsymbol{u}(\boldsymbol{x}, t). \tag{2.7}$$

The inflow condition at $x = 0$ consists of the tanh base flow (2.3) plus a periodic fluctuation $\boldsymbol{u}^\star := (u^\star, v^\star, w^\star)$,

$$u = U(y) + u^\star, \quad v = v^\star, \quad w = w^\star. \tag{2.8}$$

The fluctuation is taken to be the spatially growing eigenmode of a linear stability analysis of the mean inflow profile (see § 2.2). The fluctuation level is fixed such that the maximum amplitude of the transverse velocity perturbation is 1% of the average velocity $U_c = (U_1 + U_2)/2$ of both streams, i.e. $\max_{y,z,t} |v^\star| = 0.01 U_c$. In the transverse direction, a Dirichlet condition is enforced, i.e.

$$\boldsymbol{u}(x, \pm H/2, z, t) = U(\pm H/2)\,\hat{\boldsymbol{e}}_x. \tag{2.9}$$

This condition is consistent with the assumed base flow (2.3) at the inflow, but does not include the inlet perturbation (2.8). Therefore, H has to be chosen sufficiently large to avoid problems in the corners $(x, y) = (0, \pm H/2)$. The above 'no-penetration' condition also produces a streamwise pressure gradient because of the evolution of the shear-layer thickness, which is minimal however if H is sufficiently large. The transverse domain size was fixed at $H = 20$ after a parametric study which showed that larger domain sizes had no noticeable impact on either the flow or on the Galerkin model (Noack, Papas & Monkewitz 2002). The height chosen is comparable with the domain chosen by Comte, Silvestrini & Bégou (1998) for a large-eddy simulation of a turbulent mixing layer with the velocity ratio of 3:1. Their three-dimensional domain is 14, 28, and 140 vorticity thicknesses high, wide, and long, respectively.

The streamwise length of the computational domain is taken to be $L = 30$, corresponding to about 2 Kelvin–Helmholtz instability wavelengths. This is long

enough to capture the non-linear evolution of the flow, but short enough to avoid the first vortex pairing as observed by Comte *et al.* (1998) at about 100 shear-layer thicknesses.

At the outflow ($x = L$), finally, a convective boundary condition is employed,

$$\partial_t \boldsymbol{u} + U_c \hat{\boldsymbol{e}}_x \cdot \nabla \boldsymbol{u} = 0, \tag{2.10}$$

where the convection velocity U_c is the average $(U_1 + U_2)/2$ between the two streams. This choice is motivated by the fact that neutral linear Kelvin–Helmholtz instability waves propagate exactly with this speed while the spatially most amplified waves do so approximately (Monkewitz & Huerre 1982). This boundary condition has been successfully employed for wall-bounded shear flow in a long diffuser (Kaltenbach *et al.* 1999) and numerous other configurations.

As an initial condition, the parallel tanh base flow (2.3) plus the spatially growing eigenmode of § 2.2 is taken in the entire domain. Once initialized, the flow is found to 'forget' the initial condition after few periods and converges rapidly to a periodic solution.

For the reference simulation, a velocity ratio of $U_1/U_2 = 3$ is chosen. The velocity of the lower stream is thus large enough to sweep away the vortices in the downstream direction, but small enough to allow the vortices to evolve sufficiently within a domain of 'reasonable' length. The Reynolds number is fixed at $Re = 150$, which is large enough for the instability dynamics to be essentially inviscid, but small enough to lead to a numerically significant dissipation in the domain.

The Navier–Stokes simulation is performed in primitive variables on a staggered grid with 100, 150, and 40 cells in the streamwise, transverse, and spanwise directions, respectively. The streamwise and spanwise grid is equidistant, while the transverse grid is more dense in the shear-layer region. The Navier–Stokes terms are computed with a fourth-order-accurate finite-difference scheme. The temporal evolution employs a pressure-correction step and is second-order accurate. The spatial and temporal discretization orders were chosen according to a recommendation by Rempfer (2003) for the simulation of transitional flow. This choice was found to be a good compromise between accuracy and computational cost.

2.2. *Linear stability analysis*

A local linear stability analysis of the tanh base flow (2.3) is described which serves two purposes in the present study. On the one hand, the spatially growing eigenmode defines the periodic fluctuation for the inflow condition (2.8) of the simulation. Implicitly, the perturbation upstream of the computational box, therefore, is modelled with a linear spatial instability wave. On the other hand, the stability analysis allows the computed downstream evolution to be compared with linear stability and the role of nonlinearity to be assessed.

The local linear stability analysis is performed on the parallel tanh shear-layer profile (2.3). The eigenmode of the spatially growing fluctuation is characterized by its temporal period T, its streamwise and spanwise wavelengths λ_x and λ_z, respectively, and the streamwise spatial growth rate σ. These quantities correspond to the wavenumbers $\alpha = \alpha_r + \mathrm{i}\alpha_i = 2\pi/\lambda_x - \mathrm{i}\sigma$ and $\beta = 2\pi/\lambda_z$, and the angular frequency $\omega = 2\pi/T$. The fluctuation is written in normal-mode form

$$\boldsymbol{u}^\star = \phi(y) \exp[\mathrm{i}(\alpha x + \beta z - \omega t)], \tag{2.11}$$

with the vector-valued complex amplitude function ϕ. This eigenmode (2.11) must satisfy the incompressibility condition and the Navier–Stokes equation, linearized

Parameter	α_r	$-\alpha_i$	β	ω
$\boldsymbol{u}^\star_{2\mathrm{D}}$	0.4070	0.0845	0	0.2685
$\boldsymbol{u}^\star_{3\mathrm{D}}$	0.4150	0.0464	0.4070	0.2685

TABLE 1. Characteristic parameters of the two eigenmodes.

around the parallel base flow (2.3). The eigenmodes are computed with a standard shooting method. Details are provided in Papas, Monkewitz & Tomboulides (1999) and Papas *et al.* (2003).

Two particular eigenmodes are considered. The most amplified two-dimensional perturbation $\boldsymbol{u}^\star_{2\mathrm{D}}$ with $\beta = 0$ is used as inflow condition for the laminar shear layer of § 3. A three-dimensional perturbation $\boldsymbol{u}^\star_{3\mathrm{D}}$ is used for the transitional shear layer in § 4. The frequency $\omega_{3\mathrm{D}}$ of the three-dimensional eigenmode is taken to be equal to the frequency of the two-dimensional eigenmode $\omega_{2\mathrm{D}}$ and the spanwise wavenumber is chosen as $\beta_{3\mathrm{D}} = \alpha_{r,2\mathrm{D}}$. The characteristic parameters of the eigenmodes are shown in table 1. Note that the spatial growth of any three-dimensional eigenmode is usually smaller than that of the most amplified two-dimensional mode – as suggested by the Squire theorem.

2.3. *Galerkin model*

The starting point of the proposed Galerkin model is the 'standard' empirical Galerkin method, which we briefly summarize for later reference (see e.g. Holmes *et al.* 1998). The Galerkin approximation of the flow is based on the inner product in the space of square-integrable vector fields on the domain Ω, defined as

$$(\boldsymbol{v}, \boldsymbol{w})_\Omega := \int_\Omega \mathrm{d}V\, \boldsymbol{v} \cdot \boldsymbol{w}, \tag{2.12}$$

where $\cdot$ denotes the Euclidean product in three-dimensional Cartesian space. The corresponding norm is defined by

$$\|\boldsymbol{v}\|_\Omega := \sqrt{(\boldsymbol{v}, \boldsymbol{v})_\Omega}. \tag{2.13}$$

It should be noted that the total kinetic energy of the vector field $\boldsymbol{v}$ is given by the norm $\|\boldsymbol{v}\|^2_\Omega/2$. In the following, the symbol $\|\,\|$ without a subscript is reserved for the Euclidean norm in three-dimensional Cartesian space. In addition to these spatial operators, the Reynolds-average operator is denoted by $\langle\,\rangle$ (see the definition in Monin & Yaglom 1971). This operator represents a time-average in this study, but may also represent an ensemble-average of a transient phenomenon.

The velocity field of an empirical Galerkin model is approximated by the averaged flow $\boldsymbol{u}_0 = \langle \boldsymbol{u} \rangle$ plus an expansion with N Karhunen–Loève modes $\boldsymbol{u}_i$, $i = 1, \ldots, N$,

$$\boldsymbol{u}^{[N]}(\boldsymbol{x}, t) := \sum_{i=0}^{N} a_i(t)\, \boldsymbol{u}_i(\boldsymbol{x}), \tag{2.14}$$

where $a_0 \equiv 1$ and with the expansion coefficients $a_i := (\boldsymbol{u} - \boldsymbol{u}_0, \boldsymbol{u}_i)_\Omega$ for $i > 0$. The Karhunen–Loève modes are orthogonal with respect to the inner product (2.12),

$$(\boldsymbol{u}_i, \boldsymbol{u}_j)_\Omega = \delta_{ij}, \quad i, j = 1, 2, \ldots, N, \tag{2.15}$$

where δ_{ij} is the Kronecker symbol. The energy content of each mode is determined by the Karhunen–Loève eigenvalue,

$$\lambda_i = \left\langle (\boldsymbol{u} - \boldsymbol{u}_0, \boldsymbol{u}_i)_\Omega^2 \right\rangle = \left\langle a_i^2 \right\rangle, \quad i = 1, 2, \ldots, N. \tag{2.16}$$

More generally, the first and second moments of the expansion coefficients satisfy

$$\langle a_i \rangle = 0, \quad \langle a_i \, a_j \rangle = \lambda_i \, \delta_{ij}, \quad i, j = 1, 2, \ldots, N. \tag{2.17}$$

The Karhunen–Loève modes are computed with the snapshot method of Sirovich (1987). The snapshots are sampled equidistantly within the period T, as usual in periodic flows (see e.g. Deane *et al.* 1991 and Ma & Karniadakiks 2002). Numerical studies by the present authors reveal that the first N Karhunen–Loève modes (N even) resolve the first $N/2$ temporal harmonics, and can be computed from only $2N$ snapshots. This choice corresponds to four samples in the period of the highest resolved harmonic ($N/2$). An increase to $4N$ or $8N$ samples does not have any visible effect on the modes or resulting models. In the current study, 64 snapshots are taken. Deane *et al.* (1991) studied the periodic cylinder wake and used $M = 20$ snapshots to extract $N = 8$ Karhunen–Loève modes for the first four harmonic frequencies. This number of snapshots is 4 above the lower bound of $2N = 16$.

We emphasize that the base flow $\boldsymbol{u}_0$ used in (2.14) is the time-averaged flow and the corresponding expansion coefficient therefore remains unity, i.e. $a_0 \equiv 1$. The present study does not adopt a time-dependent $\boldsymbol{u}_0$ derived from Reynolds-stress considerations (see e.g. Aubry *et al.* 1988). That ansatz rests on a time-scale separation between fluctuations and base flow which is not justified for the present time-periodic shear layers. However, in Appendix D and also in a study of turbulent mixing layers (Noack *et al.* 2004*b*), the present authors have chosen an alternative to the use of a time-dependent $\boldsymbol{u}_0$, which consists of incorporating additional Reynolds stress contributions such as the shift mode (Noack *et al.* 2003) in the Galerkin expansion.

The evolution equation for the expansion coefficients in the Galerkin approximation (2.14) are derived by a Galerkin projection. The resulting Galerkin system is

$$\frac{\mathrm{d}}{\mathrm{d}t} a_i = \frac{1}{Re} \sum_{j=0}^{N} l_{ij} \, a_j + \sum_{j=0}^{N} \sum_{k=0}^{N} q_{ijk} \, a_j \, a_k + f_i^{\pi}(\boldsymbol{a}) \quad \text{for} \quad i = 1, \ldots, N, \tag{2.18}$$

with coefficients $l_{ij} := (\boldsymbol{u}_i, \Delta \boldsymbol{u}_j)_\Omega$ and $q_{ijk} := (\boldsymbol{u}_i, \nabla \cdot (\boldsymbol{u}_j \, \boldsymbol{u}_k))_\Omega$. The unresolved projection of the pressure term

$$f_i^{\pi} := (\boldsymbol{u}_i, -\nabla p)_\Omega \tag{2.19}$$

is based on an approximation of the pressure field p which is consistent with the Galerkin expansion (2.14). This pressure term is modelled in the next section. The need to model this term has already been anticipated by Holmes *et al.* (1998) from a Fourier space representation (see their equation 4.55).

The volume integral associated with the coefficients l_{ij} is transformed with Green's formula to reduce the differentiation order from 2 to 1. Thus, the differentiation order of the Galerkin system coefficients for the viscous and the convective term does not exceed unity. A projection of the Galerkin ansatz onto the vorticity equation (see e.g. Rempfer 1991) removes the pressure term but leads to Galerkin system coefficients with a differentiation order of 3. That order can be reduced to 2 by using the same Green's formula. The accuracy of the Galerkin system tends to decrease with increasing differentiation order in the integrals for the coefficients of the dynamical system. Although a differentiation order of 2 or more may not cause accuracy

problems with smooth data from high-order direct numerical simulations, the authors' experience indicates that it can affect the viscous term representation in the case of snapshots from second-order-accurate large-eddy simulation data.

2.4. *Pressure model*

For many 'closed' flows, the pressure term (2.19) is exactly zero (see, for instance, Holmes *et al.* 1998). An example is the model by Moehlis *et al.* (2002) for turbulent Couette flow with periodic boundary conditions in the streamwise and spanwise directions and a steady Dirichlet boundary condition in the wall-normal direction. For finite-domain approximations of open flows, however, the pressure integral generally does not vanish and may not even be negligible. In a recent wake model, Galletti *et al.* (2004) postulate a linear relationship between the pressure term and the expansion coefficients which they derive from a solution matching procedure.

The pressure term is also not negligible for the present Galerkin model of a purely convectively unstable shear layer for which an *a priori* model of the pressure integral in (2.19) is proposed.

The pressure-Poisson equation is given by

$$\Delta p = \underbrace{-\sum_{l=1}^{3}\sum_{m=1}^{3} \partial_l u^m \, \partial_m u^l}_{=:s}, \tag{2.20}$$

where u^l is the lth Cartesian component of the velocity vector $\boldsymbol{u}$ and ∂_l the partial derivate in the l-direction. The source term on the right-hand side will be denoted by s. To simplify the presentation, a homogeneous Neumann boundary condition for the pressure is assumed for the moment, i.e. the normal derivative of p in the outward direction $\boldsymbol{n}$ vanishes on the whole domain boundary $\partial\Omega$,

$$\partial_n p = \boldsymbol{n} \cdot \nabla p = 0. \tag{2.21}$$

The boundary value problem (2.20), (2.21) uniquely determines the pressure field up to a constant. Using the Galerkin approximation (2.14), the source term s (2.20) can be expressed as

$$s = \sum_{j=0}^{N}\sum_{k=0}^{N} s_{jk} \, a_j \, a_k \tag{2.22}$$

where

$$s_{jk} = -\sum_{l=1}^{3}\sum_{m=1}^{3} \partial_l u_j^m \, \partial_m u_k^l.$$

Here, the subscript indices j and k denote the expansion modes and the superscript indices l and m refer to the Cartesian component of the vector. The solution of the pressure-Poisson equation (2.20) can thus be expanded as

$$p = \sum_{j=0}^{N}\sum_{k=0}^{N} p_{jk} \, a_j \, a_k, \tag{2.23}$$

where the *partial pressures* p_{jk} satisfy

$$\Delta p_{jk} = s_{jk} \tag{2.24}$$

and the Neumann condition (2.21).

Using (2.23), the Galerkin projection of the pressure term (2.19) can now be expressed in terms of the expansion coefficients

$$(\boldsymbol{u}_i,\ -\nabla p)_\Omega = -\left(\boldsymbol{u}_i,\ \sum_{j=0}^{N}\sum_{k=0}^{N}\nabla p_{jk}\, a_j\, a_k\right)_\Omega = \sum_{j=0}^{N}\sum_{k=0}^{N} q^{\pi}_{ijk}\, a_j\, a_k, \tag{2.25}$$

where $q^{\pi}_{ijk} := -(\boldsymbol{u}_i, \nabla p_{jk})_\Omega$.

In summary, the proposed pressure model leads to an additional quadratic term in the Galerkin system (2.18),

$$\frac{\mathrm{d}}{\mathrm{d}t}a_i = \frac{1}{Re}\sum_{j=0}^{N} l_{ij}\, a_j + \sum_{j=0}^{N}\sum_{k=0}^{N}\left(q_{ijk} + q^{\pi}_{ijk}\right)\, a_j\, a_k \quad \text{for} \quad i = 1, \ldots, N, \tag{2.26}$$

which does not change its form. This remains true for a large class of boundary conditions, as shown in Appendix A. This pressure model consisting of (2.23), (2.26) will be called analytical since the Karhunen–Loève decomposition is the only empirical information employed. However, the model is not tied to the Karhunen–Loève decomposition and may be based on any other Galerkin approximation. For all Galerkin models discussed in this paper, the numerical values of the coefficients l_{ij}, q_{ijk} and q^{π}_{ijk} can be found on the website of the first author: http://vento.pi.tu-berlin.de/ts/noackbr/brn.html

A numerical realization of the pressure-term representation is detailed in Appendix B. In addition, an empirical model is proposed in Appendix C in which the linear term of the analytical representation is fitted from snapshot pressure data. No additional pressure-Poisson solutions are needed for the latter approach.

2.5. *Energy-flow analysis*

Generalizing a framework established by Rempfer (1991), the total and modal energy balance equations are derived. The derivation is based on the Reynolds decomposition of the flow $\boldsymbol{u}$ into a mean flow $\boldsymbol{u}_0$ and a fluctuation $\boldsymbol{u}'$,

$$\boldsymbol{u} = \boldsymbol{u}_0 + \boldsymbol{u}' \tag{2.27}$$

of transient flow. For convenience, the fluctuation is assumed to be represented exactly by a finite Galerkin approximation,

$$\boldsymbol{u}' = \sum_{i=1}^{N} a_i\, \boldsymbol{u}_i. \tag{2.28}$$

This assumption can later be relaxed by taking the limit $N \to \infty$.

The total energy balance equation for the domain is obtained by multiplying the Navier–Stokes equation (2.5) with $\boldsymbol{u}'$, integrating over the domain and manipulating the terms (see, for instance, Monin & Yaglom 1971). The evolution of the turbulent kinetic energy, defined by

$$\mathscr{K} = \tfrac{1}{2}\langle(\boldsymbol{u}', \boldsymbol{u}')_\Omega\rangle = \int_\Omega \mathrm{d}V\, \tfrac{1}{2}\langle\|\boldsymbol{u}'\|^2\rangle, \tag{2.29}$$

satisfies the energy balance equation

$$\frac{\mathrm{d}}{\mathrm{d}t}\mathscr{K} = \mathscr{P} + \mathscr{D} + \mathscr{C} + \mathscr{T} + \mathscr{F}, \tag{2.30}$$

where the production $\mathscr{P}$, the dissipation $\mathscr{D}$, the convection term $\mathscr{C}$, the transfer term $\mathscr{T}$, and the pressure power $\mathscr{F}$ are

$$\mathscr{P} = -\langle(\boldsymbol{u}', \nabla\cdot(\boldsymbol{u}'\boldsymbol{u}_0))_\Omega\rangle = -\int_\Omega \mathrm{d}V \sum_{l=1}^{3}\sum_{m=1}^{3}\langle u'^{,l}\boldsymbol{u}'^{,m}\rangle\partial_m u_0^l,$$

$$\mathscr{D} = \frac{1}{Re}\langle(\boldsymbol{u}', \Delta\boldsymbol{u}')_\Omega\rangle = \frac{1}{Re}\int_\Omega \mathrm{d}V\langle\boldsymbol{u}'\cdot\Delta\boldsymbol{u}'\rangle,$$

$$\mathscr{C} = -\langle(\boldsymbol{u}', \nabla\cdot(\boldsymbol{u}_0\boldsymbol{u}'))_\Omega\rangle = -\int_{\partial\Omega} \mathrm{d}\boldsymbol{A}\cdot\boldsymbol{u}_0\tfrac{1}{2}\langle\|\boldsymbol{u}'\|^2\rangle,$$

$$\mathscr{T} = -\langle(\boldsymbol{u}', \nabla\cdot(\boldsymbol{u}'\boldsymbol{u}'))_\Omega\rangle = -\int_{\partial\Omega} \mathrm{d}\boldsymbol{A}\cdot\left\langle\boldsymbol{u}'\tfrac{1}{2}\|\boldsymbol{u}'\|^2\right\rangle,$$

$$\mathscr{F} = -\langle(\boldsymbol{u}', \nabla p)_\Omega\rangle = -\int_{\partial\Omega} \mathrm{d}\boldsymbol{A}\cdot\langle\boldsymbol{u}'p'\rangle.$$

Typically, $\mathscr{D}$ is decomposed into a volume and a surface integral (see for instance Monin & Yaglom 1971). This is not done in the present study, since no additional insight is gained from this decomposition.

Analogously, a balance equation for the ith Karhunen–Loève mode is derived. The Navier–Stokes equation is multiplied with the Galerkin contribution $a_i\,\boldsymbol{u}_i$ as opposed to the complete fluctuation $\boldsymbol{u}'$. This projection uses the Galerkin system (2.18), the Galerkin approximation (2.28), the attractor properties (2.17), and leads to

$$\frac{\mathrm{d}}{\mathrm{d}t}\mathscr{K}_i = \mathscr{P}_i + \mathscr{D}_i + \mathscr{C}_i + \mathscr{T}_i + \mathscr{F}_i, \tag{2.31}$$

with

$$\mathscr{K}_i = \tfrac{1}{2}\left\langle\left(a_i\boldsymbol{u}_i, \sum_{j=1}^{N} a_j\boldsymbol{u}_j\right)_\Omega\right\rangle = \tfrac{1}{2}\lambda_i,$$

$$\mathscr{P}_i = -\left\langle\left(a_i\boldsymbol{u}_i, \nabla\cdot\left(\sum_{j=1}^{N} a_j\boldsymbol{u}_j\boldsymbol{u}_0\right)\right)_\Omega\right\rangle = q_{ii0}\lambda_i,$$

$$\mathscr{D}_i = \frac{1}{Re}\left\langle\left(a_i\boldsymbol{u}_i, \Delta\sum_{j=1}^{N} a_j\boldsymbol{u}_j\right)_\Omega\right\rangle = \frac{1}{Re}l_{ii}\lambda_i,$$

$$\mathscr{C}_i = -\left\langle\left(a_i\boldsymbol{u}_i, \nabla\cdot\left(\boldsymbol{u}_0\sum_{j=1}^{N} a_j\boldsymbol{u}_j\right)\right)_\Omega\right\rangle = q_{i0i}\lambda_i,$$

$$\mathscr{T}_i = -\left\langle\left(a_i\,\boldsymbol{u}_i, \nabla\cdot\left(\sum_{j=1}^{N} a_j\boldsymbol{u}_j\sum_{k=1}^{N} a_k\,\boldsymbol{u}_k\right)\right)_\Omega\right\rangle = \sum_{j=1}^{N}\sum_{k=1}^{N} q_{ijk}\langle a_i a_j a_k\rangle,$$

$$\mathscr{F}_i = -\langle(a_i\boldsymbol{u}_i, \nabla p)_\Omega\rangle = \sum_{j=0}^{N}\sum_{k=0}^{N} q^{\pi}_{ijk}\langle a_i a_j a_k\rangle.$$

Note that the pressure-power term contains products with $a_0 = 1$, i.e. this term could be decomposed into a quadratic and a cubic term, while the linear term vanishes due to (2.17).

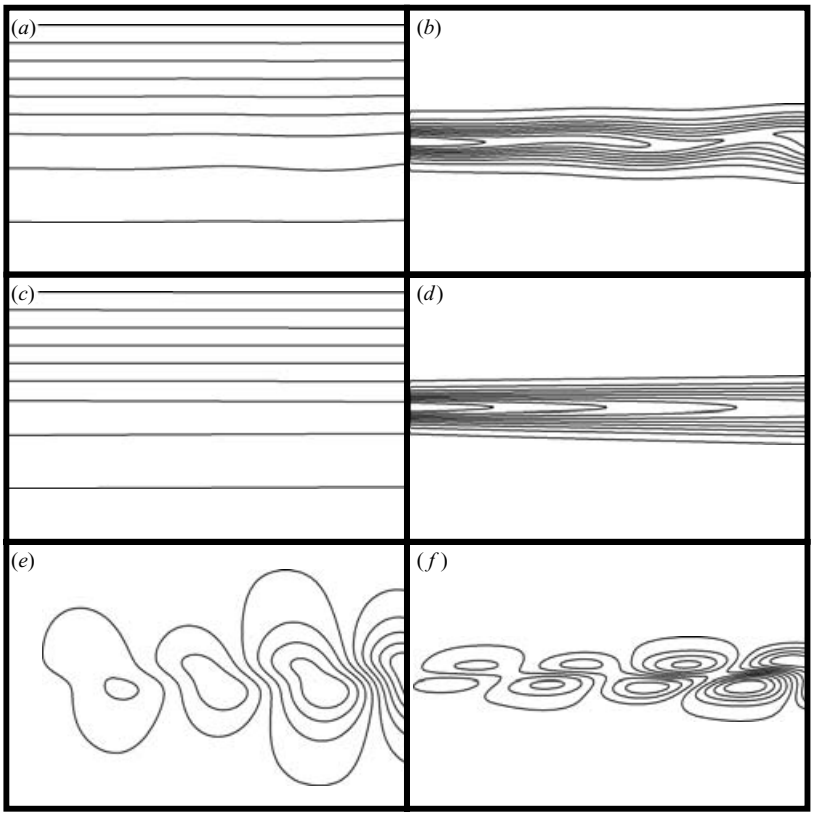

FIGURE 2. Navier–Stokes simulation for the reference conditions: streamlines (a, c, e) and iso-vorticity contours (b, d, f) of the instantaneous flow (a, b), the time-averaged flow (c, d), and of the instantaneous fluctuation (e, f). The displayed region is the computational domain $0 \leqslant x \leqslant 30$, $-10 \leqslant y \leqslant 10$.

For the time-averages, the left-hand side of (2.31) vanishes, and the remaining equation may be considered as a Kirchhoff rule for the energy flow to each mode – in analogy to the currents in an electric network. It should be noted that the formulation guarantees the additivity of the modal contributions to the total of each term in (2.30),

$$\mathscr{K} = \sum_{i=1}^{N} \mathscr{K}_i, \quad \mathscr{P} = \sum_{i=1}^{N} \mathscr{P}_i, \quad \mathscr{D} = \sum_{i=1}^{N} \mathscr{D}_i, \quad \mathscr{C} = \sum_{i=1}^{N} \mathscr{C}_i, \quad \mathscr{T} = \sum_{i=1}^{N} \mathscr{T}_i, \quad \mathscr{F} = \sum_{i=1}^{N} \mathscr{F}_i. \tag{2.32}$$

3. The two-dimensional laminar shear layer

In this section, the two-dimensional laminar shear layer is studied. In § 3.1, the Navier–Stokes solution is computed and analysed. A low-dimensional model of this simulation is proposed in § 3.2. In § 3.3, an energy-flow analysis elucidates the observations of § 3.2.

3.1. *Navier–Stokes simulation*

Figure 2 displays the Navier–Stokes solution, including its Reynolds decomposition. Since the averaged flow remains nearly parallel, the fluctuation level can be considered

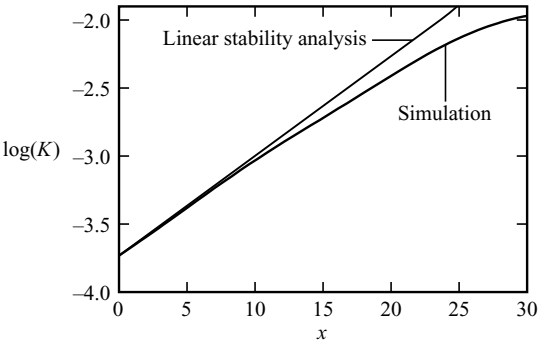

FIGURE 3. Streamwise evolution of the turbulent kinetic energy (3.1). The thick curve corresponds to the reference simulation of figure 2. The thin straight line is the exponential spatial growth associated with the linear instability of the inlet profile.

to be small. Furthermore the fluctuation streamlines and iso-vorticity curves closely resemble those of the linear eigenmode used as inflow boundary condition (see § 2.2). The spatial growth of the fluctuation is characterized by the streamwise evolution of the turbulent kinetic energy, integrated across the shear layer

$$K(x) := \int \mathrm{d}y \tfrac{1}{2}\langle \|\boldsymbol{u}'(x, y, t)\|^2 \rangle. \tag{3.1}$$

As it should be, the spatial growth of the fully nonlinear simulation initially agrees well with the prediction of linear stability theory for the inflow profile (see figure 3).

It should be borne in mind that the flow under consideration is purely convectively unstable and has no regions of absolute instability – in contrast to some wall-bounded shear layers (Wee *et al.* 2002). This property qualifies the flow for parabolized stability approaches (Bertolotti, Herbert & Spalart 1992), but no global empirical Galerkin models seem to exist without simplifying assumptions, e.g. streamwise periodicity, and without heuristic elements, e.g. additional eddy viscosities.

3.2. *Galerkin model*

In the following, two Galerkin models are compared: model A with the pressure term neglected, and model B with the proposed analytical pressure representation.

In figures 4 and 5, the modes and corresponding eigenvalues of the Karhunen–Loève decomposition are displayed. The modes form pairs ($\boldsymbol{u}_1$, $\boldsymbol{u}_2$), ($\boldsymbol{u}_3$, $\boldsymbol{u}_4$), etc., with similar energy, frequency and streamwise wavenumbers. The energy decreases from pair to pair in a rapid geometric progression, and the frequency and wavenumber of the nth mode pair ($\boldsymbol{u}_{2n-1}$, $\boldsymbol{u}_{2n}$) are $n\omega$ and $n\alpha$ of the Kelvin–Helmholtz wave, respectively. More precisely, the transverse velocity fluctuation of modes $i = 1, 2, 3, 4, \ldots$ are locally well approximated by the travelling waves $\cos(\omega t - \alpha x)$, $\sin(\omega t - \alpha x)$, $\cos 2(\omega t - \alpha x)$, $\sin 2(\omega t - \alpha x)$, etc.

The first four modes already contain 99.99% of the total turbulent kinetic energy. This high accuracy of the low-dimensional flow representation is due to the small amplitude of the primary Kelvin–Helmholtz wave which barely excites higher harmonics. For periodic shear flows with an absolute instability, the accuracy tends to be smaller, but is still surprisingly high. An example is the laminar vortex shedding behind the circular cylinder at $Re = 100$, where six modes are needed for a 99.96% resolution of the turbulent kinetic energy (Deane *et al.* 1991).

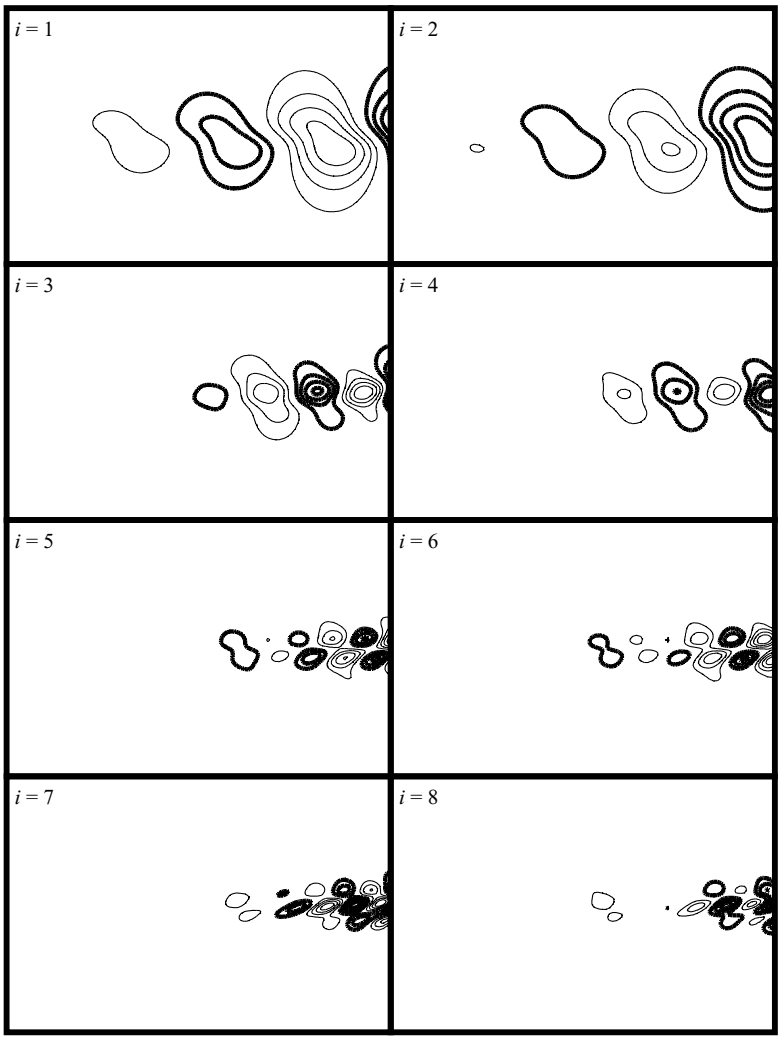

FIGURE 4. Streamlines of the first eight Karhunen–Loève modes of the reference simulation displayed in figure 2. Positive (negative) values of the streamfunction are indicated by thick (thin) lines. The displayed region is the computational domain $0 \leqslant x \leqslant 30$, $-10 \leqslant y \leqslant 10$.

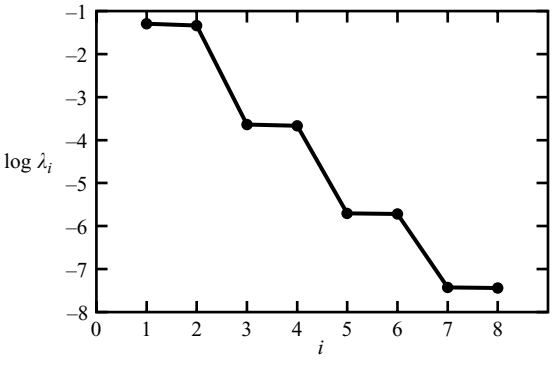

FIGURE 5. Karhunen–Loève eigenvalues λ_i as function of the mode number i.

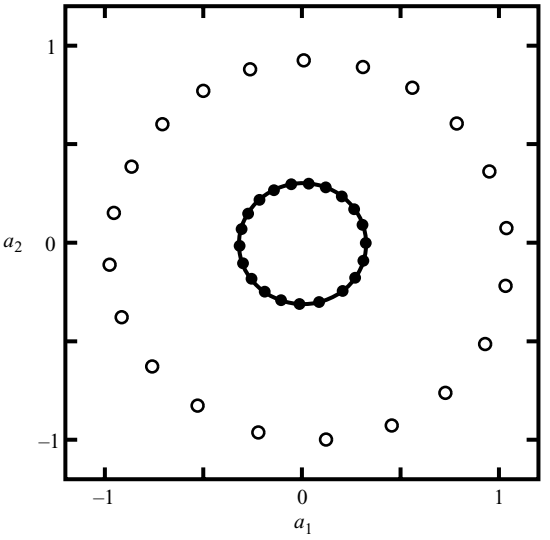

FIGURE 6. The attractors of Galerkin models A (○) and B (●). The solid line represents the Navier–Stokes simulation.

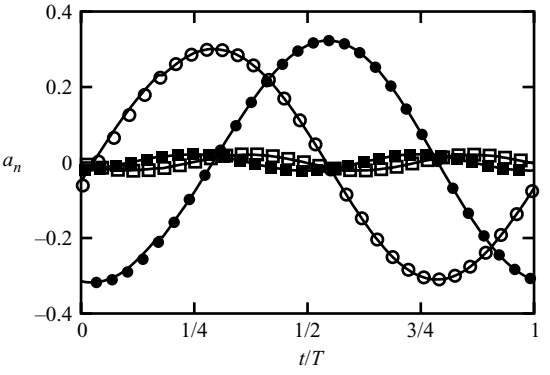

FIGURE 7. The first four expansion coefficients a_1 (●), a_2 (○), a_3 (■), and a_4 (□) of Galerkin model B versus time measured in periods T. The solid lines represent the Navier–Stokes simulation.

The results suggest a truncation of the Galerkin approximation at $N = 4$. Figure 6 displays the attractors of the Galerkin systems A and B. While system B accurately reproduces the limit cycle of the Galerkin approximation of the Navier–Stokes solution, the amplitude of system A is more than three times too large. It may not be surprising that a Galerkin system is more accurate if the full evolution equation including the pressure term is incorporated, but such a large effect of neglecting the pressure term has, to our knowledge, not been reported previously. It will be elucidated later in the framework of an energy-flow analysis (§ 3.3).

Figure 7 illustrates the temporal behaviour of Galerkin system B. The Galerkin solution is seen to coincide perfectly with the corresponding expansion coefficients of the Navier–Stokes simulation. The temporal evolution of the first four coefficients is consistent with the travelling wave picture mentioned above, where a_1, a_2, a_3, a_4 have frequencies $\omega, \omega, 2\omega, 2\omega$, respectively, with a 90° phase shift within each pair.

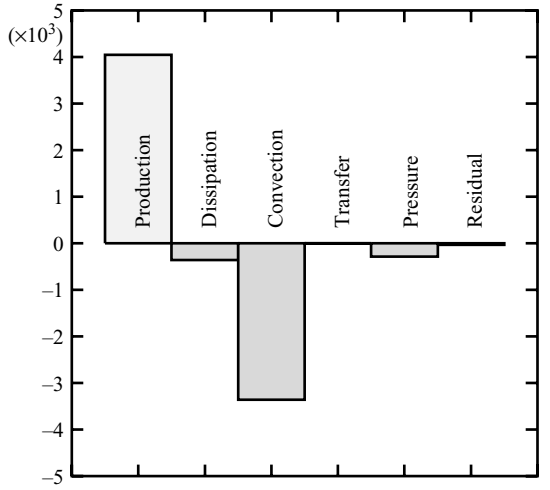

FIGURE 8. Histogram with the time-averaged total energy contributions of, from left to right, production $\mathscr{P}$, dissipation $\mathscr{D}$, convection $\mathscr{C}$, transfer $\mathscr{T}$, pressure power $\mathscr{F}$ and their sum $\mathscr{P}+\mathscr{D}+\mathscr{C}+\mathscr{T}+\mathscr{F}$.

The focus of the present study is on modelling the limit-cycle dynamics. A numerical investigation of the two- and three-dimensional shear layers indicates that the limit cycle has a large range of attraction in Galerkin phase space. Any transient Galerkin solution approaches that limit cycle, provided that the initial condition is not orders of magnitude away from the attractor. The transient times, however, are unrealistically large. This aspect is briefly discussed in Appendix D and will be the subject of a separate publication. The transient behaviour can be properly described in the framework of empirical Galerkin models at the expense of significantly increasing the number of modes (Ma & Karniadakis 2002; Jørgensen, Sørensen & Brøns 2003; Noack *et al.* 2003; Bergmann, Cordier & Brancher 2004). The proposed pressure-term representation can also be incorporated in these empirical Galerkin models, generalized for transient dynamics, since the kinematics is still described by the Galerkin ansatz (2.14).

3.3. *Energy-flow analysis*

A total and modal energy-flow analysis of the Navier–Stokes solution, as described in § 2.5, is carried out. The corresponding analysis of the Galerkin model with $N=4$ yields almost identical results.

In figure 8, the five contributions to the change of turbulent kinetic energy are visualized for the periodic flow. The production is the only source of energy. About 82% of this energy flow is convected across the domain boundary, about 9% is dissipated and about 9% is lost across the boundary by pressure power. The transfer term is negligible. The large loss due to convection characterizes convectively unstable flow. In contrast, convection is small for equilibrium wall-bounded flows, e.g. channel flow. The dissipation and pressure power are equally important as energy sinks. This explains why neglecting the pressure term in Galerkin model A gives rise to larger amplitudes. It is noted that even small neglected energy terms can give rise to large changes in the Galerkin solutions, since all energy terms (except for the transfer term) scale with the square of the amplitude. The transfer term has a damping effect, since it transfers energy from the first to higher harmonics where the energy dissipation

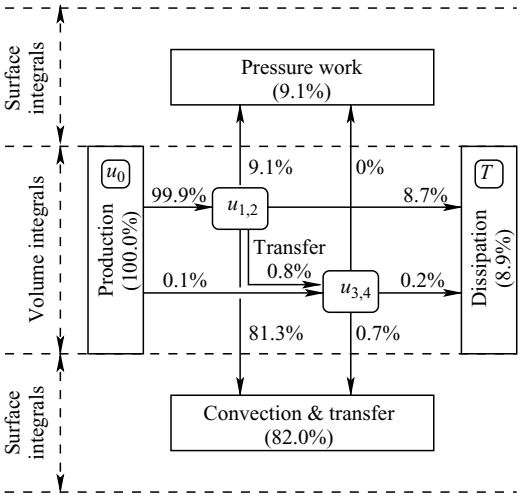

FIGURE 9. Modal energy-flow diagram of the laminar shear layer involving the first two pairs of Karhunen–Loève modes, the average flow u_0 and thermal energy T. The arrows point in the direction of the energy flow. The kind of the energy flow is denoted by the four rectangular boxes, in which the total transferred percentages are indicated. On the left, it is also indicated which energy exchanges across the boundary correspond to surface or volume integrals.

is more efficient. Thus, the transfer term becomes more important when the higher harmonics are excited.

The above energy terms are decomposed into their modal contributions in figure 9. Here, the mode pairs $(\boldsymbol{u}_{2n-1}, \boldsymbol{u}_{2n})$ with the same frequency are grouped into two compound modes $\boldsymbol{u}_{1,2}$ and $\boldsymbol{u}_{3,4}$. For instance, the production due to $\boldsymbol{u}_{1,2}$ is $\mathscr{P}_1 + \mathscr{P}_2$. The total energy terms are quantified in the boxes of figure 8. These terms are the sums of the modal contributions indicated by arrows away from or towards the boxes, depending on the sign of the contributions. According to the Kirchhoff-type rules (2.30), (2.31), the sum of all total energy-flow terms, as well as the corresponding sum for each mode, must vanish.

The transfer term from modes $\boldsymbol{u}_{1,2}$ to $\boldsymbol{u}_{3,4}$ is simply the sum $\mathscr{T}_1 + \mathscr{T}_2$ or $-\mathscr{T}_3 - \mathscr{T}_4$, since the higher-order modes play no role. In general, however, the energy transfer results from a triadic interaction, i.e. involves three (compound) modes and cannot be represented as easily by an arrow.

Figure 9 reveals that the contribution of $\boldsymbol{u}_{3,4}$ to each total energy-flow term is less than 1% of the total production. Yet, these modes cannot be neglected in the Galerkin model without inducing severe inaccuracies (see Noack *et al.* 2002). This sensitivity is consistent with the observation that a high-order numerical accuracy is required for the Navier–Stokes simulation, the Galerkin approximation, and the Galerkin projection.

The energetic terms of modes 3 and 4 increase with the fluctuation level, since the energy transfer from modes 1 and 2 is enhanced by nonlinearity. However, the important role of the pressure term is also observed at larger fluctuation levels. Raising the inflow fluctuation by a factor of 5 increases the pressure power by 377%. When normalized with the production, however, the pressure power decreases by 49.6%. This decrease seems mostly caused by the near saturation of the Kelvin–Helmholtz vortices at the outflow boundary and less related to the increased nonlinearity. Current investigations of direct numerical simulations of laminar and transitional cylinder wakes as well as large-eddy simulations of turbulent mixing layers indicate a strong correlation

between the pressure power and the growth of the fluctuation at the outflow boundary.

In summary, the energy-flow analysis elucidates which terms of the Navier–Stokes equation play an energetically important role, and which modes are needed to resolve the energy flows with a given accuracy.

4. Three-dimensional transitional shear layer

As a next step, the low-dimensional modelling procedure is generalized to three-dimensional shear layers. The organization of this section is analogous to the previous one.

4.1. *Navier–Stokes simulation*

The inlet condition for the three-dimensional Navier–Stokes simulation is the most amplified spatially growing linear eigenmode described in § 2.2. This eigenmode is a Kelvin–Helmholtz wave travelling in an oblique direction about 46° away from the free-stream direction. For reasons of symmetry, this oblique wave may be inclined in the positive or negative spanwise direction, i.e. (2.11) gives rise to two modes denoted by the superscripts $\pm$:

$$\boldsymbol{u}^{\pm}(x, y, z, t) = \phi^{\pm}(y) \exp[\mathrm{i}(\alpha x \pm \beta z - \omega t)].$$

As inlet fluctuation, the sum of both eigenmodes, corresponding to a stationary spanwise modulation of the inlet perturbation, is chosen

$$\boldsymbol{u}^{\star} = A_{BC}(\boldsymbol{u}^{+} + \boldsymbol{u}^{-}). \tag{4.1}$$

The amplitude A_{BC} is normalized to yield a fluctuation with a maximum transverse velocity of $0.01\,U_c$ in analogy to § 3. This choice of boundary condition gives rise to the well-studied spanwise cells of Kelvin–Helmholtz-like vortices with adjacent cells of opposite phase. These particular cells have been chosen to make the inlet condition sufficiently different from the two-dimensional case. The goal here is to monitor the effect of three-dimensionality on the Galerkin model and on the energy flows. Figure 10 depicts a snapshot of the Navier–Stokes solution which preserves the time-periodicity of the inlet condition in the domain considered. The spatial growth of this solution follows the predictions of linear stability theory over one Kelvin–Helmholtz wavelength before nonlinear effects decrease the growth further downstream – in analogy to § 3.

4.2. *Galerkin model*

Again, the Galerkin models A and B without and with pressure-term representation are compared for the three-dimensional simulation of § 4.1.

In analogy to the corresponding two-dimensional flow, the Karhunen–Loève decomposition of the simulation leads to pairs of modes. As before, the nth pair resolves the nth harmonic $n\omega$ with characteristic streamwise wavenumber of $n\alpha$. The Karhunen–Loève modes are composed of Fourier modes in the spanwise direction with zero spanwise average, and hence produce a spanwise variation of the mean flow by nonlinear interactions. The first two modes are found to resolve 99.4% of the turbulent kinetic energy. The residual energy of a four-mode expansion is less than 0.5×10^{-6}.

Figure 11 displays the attractors of Galerkin models A and B. The latter system again follows the Navier–Stokes solution with high accuracy: better than 1×10^{-6} in terms of fluctuation amplitude and frequency. Unlike the two-dimensional case, the omission of the pressure-term representation now leads to an amplitude error of only 12% compared to a factor of 3.

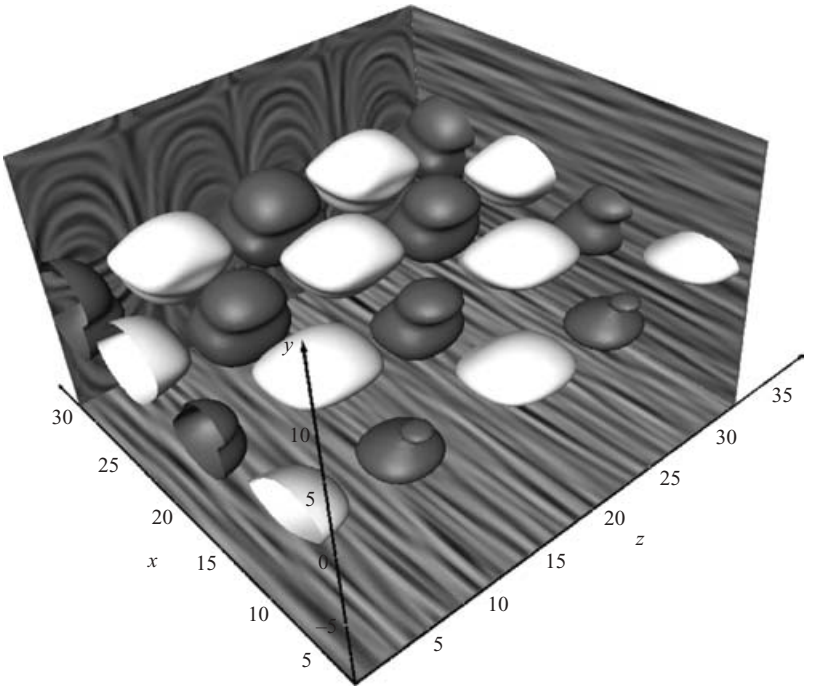

FIGURE 10. Snapshot of a three-dimensional simulation. The surfaces correspond to $v = 0.005$ (dark) and $v = -0.005$ (bright). The background on $x = 30$, $y = -10$ and $z = 2\lambda_z$ displays the flow on planes by elongating white and dark spots as 'quasi streamlines' along the tangential velocity. The data region corresponds to the computational domain doubled in the spanwise direction.

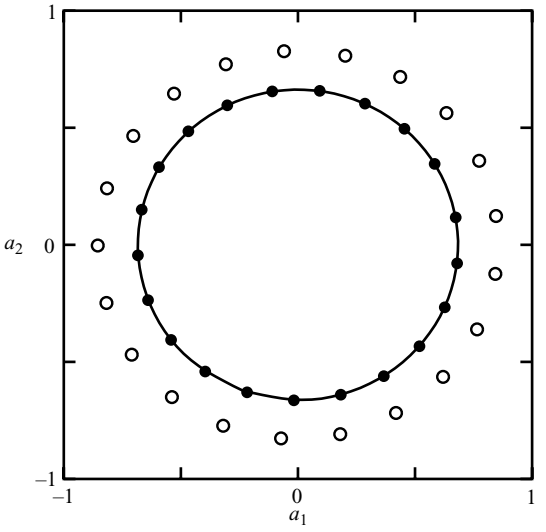

FIGURE 11. Same as figure 6, but for the attractors of Galerkin models A (○) and B (●) associated with the three-dimensional flow.

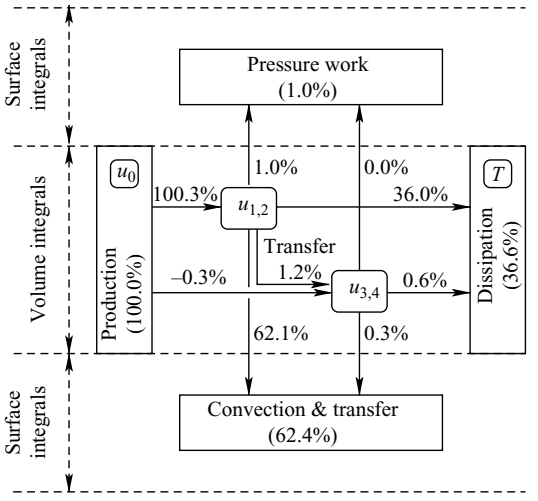

FIGURE 12. Same as figure 9, but for the three-dimensional shear layer.

Apparently, three-dimensionality mitigates the role of the pressure term in the Galerkin model. The same tendency is observed with increased levels of fluctuation, either by adopting larger inlet perturbations or by increasing the streamwise domain size. This tendency may explain why Wee *et al.* (2002) can neglect the pressure term for the flow over a backward-facing step at a Reynolds number of 5000. The reason for the difference between two- and three-dimensional flows is elucidated by the energy-flow consideration of the following section.

4.3. *Energy-flow analysis*

The result of the modal energy-flow analysis is visualized in figure 12. The relative energy flows between the modes are comparable with their two-dimensional analogues in figure 9. In both cases, the production associated with the second mode pair ($i = 3, 4$) is about three orders of magnitude smaller than that of the first pair ($i = 1, 2$). Moreover, the production of the second pair is negative, for which no explanation can be offered at this point.

The dissipation plays a larger role than in the two-dimensional flow due to spanwise 'friction' between neighbouring cells of opposite phase. The pressure power still acts as an energy sink. Yet, its magnitude decreases from 9.2% in § 3 to only 1.0% of the total production. This change reflects the fact that the omission of the pressure term leads to an error which is one order of magnitude smaller than in the two-dimensional case. In other simulations with different domains and different inlet conditions, the relative error of the Galerkin model A has been found to be strongly correlated with the relative role of pressure power.

The reduced surface integral of pressure power in the three-dimensional case corresponds to a significantly reduced pressure fluctuation level. Loosely speaking, this may be explained by the fact that less pressure gradient is required to 'push' fluid from one point to another because fluid motion is no longer constrained to the (x, y)-plane. In contrast, the fluctuation level of the streamwise velocity at the outflow differs by less than 10% between the two- and three-dimensional shear layers. To a much lesser extent, the pressure power is also reduced by a somewhat lower correlation between pressure and velocity fluctuations at the outflow.

5. Conclusions

In the present study, the role of the pressure integral in empirical Galerkin models of standard, spatially evolving shear layers is investigated. To be able to truncate the model at very low order (at 4 modes), the inlet fluctuation level was chosen sufficiently small so that a nonlinear numerical Navier–Stokes simulation initially follows the exponential growth of the linear instability wave used as an inflow condition.

The simulation is subjected to a low-dimensional Karhunen–Loève decomposition and a detailed energy-flow analysis for each mode and each Navier–Stokes term. Based on the Karhunen–Loève decomposition, an empirical Galerkin model is formulated with and without pressure-term representation. The role of the pressure term in open flows has been elucidated by a number of authors. One heuristic approach consists of adding heuristic forcing terms to the Galerkin projection of the Navier–Stokes equation (see, for instance, Aubry *et al.* 1988). An often practised approach consists of 'escaping' into the pressure-free vorticity transport equation (Rempfer 1991; Noack & Eckelmann 1994). This avoidance of the pressure modelling task has two costs. First, the energy residuum of the Navier–Stokes simulation is unknown and cannot be used to assess the quality of the simulation and the Galerkin model. Second, the numerical errors are increased due to the higher-order spatial derivatives and the mass-matrix for the temporal vorticity derivative.

The Karhunen–Loève decomposition of the two- and three-dimensional shear layers considered here yields pairs of modes, with the first pair resolving more than 99%, and the first two pairs more than 99.9% of the turbulent kinetic energy in both cases. This justified the truncation of the model at two pairs of modes. The analysis of the total energy flow of each type has elucidated the role of production, dissipation, convection, transfer and pressure power. As in non-equilibrium spatially evolving flows, the only source of turbulent kinetic energy is the production, and the dominant energy 'sink' is the convection out of a finite domain.

The principal finding of the study is that the pressure power can be as important as dissipation. If a representation of the pressure term is incorporated in the model, very accurate results are obtained for the relatively simple shear layer considered here with only four Karhunen–Loève modes. The lack of a pressure-term model, on the other hand, typically gives rise to important amplitude errors which cannot be compensated by an increase in the number of modes. The amplitude error can be one or two orders of magnitude larger than the relative energy-term error. Neglecting the second pair of Karhunen–Loève modes which resolves less than 1% of all energy-flow terms (compared to total production) even gives rise to a diverging Galerkin solution. Furthermore, truncation errors of the second-order spatial discretization of the Navier–Stokes simulation or the Galerkin projection easily accumulate to a $\sim$1% energy residuum in the total balance equation of turbulent kinetic energy. The large sensitivity of the Galerkin solution to small neglected energy flows may be a characteristic feature of purely convectively unstable shear layers. According to the authors' experience, the sensitivity is typically smaller for other flows. For absolutely unstable wake flows, for instance, the relative amplitude error is comparable to the relative level of unresolved fluctuation energy.

In summary, the main methodological contribution of the present study is an analytically derived pressure-term representation for empirical Galerkin models. This pressure model does not require additional empirical information and does not change the form of the Galerkin system.

The secondary finding of this study concerns the effect of three-dimensionality, which appears to have a mitigating effect on the error made by neglecting the pressure term. Thus, omission of the pressure term leads to larger-amplitude errors in Galerkin solutions for two-dimensional flow. In addition, large fluctuation levels at the inflow have also been seen to reduce the error of the limit-cycle amplitude.

The work has been partially funded by the Deutsche Forschungsgemeinschaft (DFG) under grant NO 258/1-1 and by ERCOFTAC. B. R. N. acknowledges funding and excellent working conditions of the Collaborative Research Centre 557 'Control of complex turbulent flow' which is supported by the DFG and hosted at the Technical University Berlin. Stimulating discussions with Andrzej Banaszuk, Fabio Bertolotti, Pierre Comte, Laurent Cordier, Ahmed Ghoniem, Phil Holmes, Eckart Meiburg, and Dietmar Rempfer are acknowledged. The low-dimensional modelling and control team at the Technische Universität Berlin – in particular Andreas Dillmann, Rudibert King, Johannes Gerhard, Mandy Goltsch, Mark Pastoor, Ivanka Pelivan, Michael Schlegel, and Tino Weinkauf – has always been a source of valuable advice and inspiration. The three-dimensional flow visualization has been prepared with Amira 3.0 (http://amira.zib.de). Angela Pätzold has helped us in numerous computer and software related tasks. Last but not least, we thank the referees for their helpful suggestions.

Appendix A. Analytical pressure model for general boundary conditions

In this section, the form of the analytical pressure model is shown to be preserved for a large class of boundary conditions. At a stationary wall, for instance, the boundary condition can be derived from the Navier–Stokes equation,

$$\partial_n p = \frac{1}{Re}\, \boldsymbol{n} \cdot \Delta \boldsymbol{u}. \tag{A 1}$$

Substitution of (2.14) in (A 1) leads to an inhomogeneous Neumann condition

$$\partial_n p = \sum_{j=0}^{N} s_j\, a_j, \tag{A 2}$$

where $s_j = Re^{-1}\, \boldsymbol{n} \cdot \Delta \boldsymbol{u}_j$. The linear inhomogeneity of (A 2) with respect to $\boldsymbol{a}$ seems to be inconsistent with the simultaneous quadratic dependency of the pressure expansion on the expansion coefficients. Fortunately, this inconsistency can be removed by transforming (A 2) with a trick of analytic geometry,

$$\partial_n p = (1, a_1, \ldots, a_N) \begin{pmatrix} s_0 & \frac{1}{2}s_1 & \cdots & \frac{1}{2}s_N \\ \frac{1}{2}s_1 & 0 & \cdots & 0 \\ \vdots & \ddots & & \vdots \\ \frac{1}{2}s_N & 0 & \cdots & 0 \end{pmatrix} \begin{pmatrix} 1 \\ a_1 \\ \vdots \\ a_N \end{pmatrix}. \tag{A 3}$$

Now, the pressure expansion (2.23), the pressure source term (2.22), and the von Neumann inhomogeneity of (A 3) are quadratic forms in $\boldsymbol{a} = (1, a_1, \ldots, a_N)$. The following boundary condition for the partial pressure p_{jk}:

$$\partial_n p_{jk} = \begin{cases} s_0 & \text{if } j, k = 0, \\ \frac{1}{2}s_j & \text{if } j > 0,\ k = 0, \\ \frac{1}{2}s_k & \text{if } j = 0,\ k > 0, \\ 0 & \text{if } j, k > 0, \end{cases} \tag{A 4}$$

implies that the expansion (2.23) satisfies the boundary condition (A 3), or, equivalently, (A 2).

The most general boundary condition for the pressure in a stationary domain can be derived from the Navier–Stokes equation,

$$\partial_n p = \boldsymbol{n}\cdot\nabla p = \boldsymbol{n}\cdot\left[-\partial_t \boldsymbol{u} - \nabla\cdot(\boldsymbol{u}\boldsymbol{u}) + \frac{1}{Re}\,\Delta\boldsymbol{u}\right]. \tag{A 5}$$

For a steady realization of this boundary condition, the construction of partial pressures, which respect this boundary condition and the quadratic form of the pressure model, follows along the same lines. For the unsteady convective outflow condition, the time-derivative of the velocity in (A 5) has to be replaced using (2.10). The Galerkin representation of the resulting term again assumes the desired quadratic form. The incorporation of different boundary conditions in the same pressure model is readily carried out since the form does not change.

Appendix B. Numerical computation of the analytical pressure model

In this Appendix, a numerical algorithm for the computation of the pressure model is proposed. This algorithm has several advantages over the direct computation of the partial pressures. In fact, the pressure model is obtained using the same pressure-correction step as the Navier–Stokes solver.

Let p_0 be the pressure associated with the base flow $\boldsymbol{u}=\boldsymbol{u}_0$, $p_j^{\pm}$ be associated with $\boldsymbol{u}_j^{\pm}=\boldsymbol{u}_0\pm\boldsymbol{u}_j$, $j=1,2,\ldots,N$ and p_{jk}^0 correspond to $\boldsymbol{u}_{jk}^0=\boldsymbol{u}_0+\boldsymbol{u}_j+\boldsymbol{u}_k$, $1\leqslant j<k\leqslant N$. Note that each of these velocity fields satisfies the boundary condition of the direct numerical simulation with suitable amplitude and phase of the inlet condition. Hence, each associated pressure field can be computed from a pressure-correction step, advancing the phase in proportion to the chosen time step.

The pressure integral (2.25) yields $N^2\,(N+1)/2$ equations,

$$\begin{aligned}
q_i &:= (u_i, -\nabla p_0)_\Omega = q^\pi_{i00}\\
q^\pm_{ij} &:= (u_i, -\nabla p^\pm_i)_\Omega = q^\pi_{i00} \pm q^\pi_{i0j} + q^\pi_{ijj},\\
q^0_{ijk} &:= \left(u_i, -\nabla p^0_{jk}\right)_\Omega = q^\pi_{i00} + q^\pi_{i0j} + q^\pi_{i0k} + q^\pi_{ijj} + q^\pi_{ikk} + q^\pi_{ijk},
\end{aligned}$$

where the quantities q_i, $q^\pm_{ij}$, and q^0_{ijk} have been introduced for convenience. Thus, a linear system of equations for $N^2\,(N+1)/2$ coefficients is defined, assuming $q^\pi_{ijk}=0$ at $j>k$.

These coefficients can be obtained from a simple recursion scheme at $i=1,2,\ldots,N$, $j=1,2,\ldots,N$ and $k=j,j+1,\ldots,N$:

$$\begin{aligned}
q^\pi_{i00} &= q_i,\\
q^\pi_{i0j} &= \frac{q^+_{ij}-q^-_{ij}}{2},\\
q^\pi_{ijj} &= \frac{q^+_{ij}+q^-_{ij}}{2} - q_i,\\
q^\pi_{ijk} &= q^0_{ijk} - q^\pi_{i00} - q^\pi_{i0j} - q^\pi_{i0k} - q^\pi_{ijj} - q^\pi_{ikk}.
\end{aligned}$$

This recursion procedure has several advantages over the direct partial-pressure computation: First, the recursion procedure does not require the development of another Poisson solver in addition to that of the pressure-correction scheme. Second, the analytical formulation of a different boundary condition does not need to be

re-considered, since the quadratic form is rigorously derived. And finally, the direct computation is numerically found to be not well-conditioned for iteration schemes. Instead of over-relaxation schemes, inefficient under-relaxation techniques have to be employed. The efficiency and accuracy of the recursion procedure is found to be significantly better.

As an aside, the computation of Galerkin coefficients l_{ij}, $q_{ijk} + q^{\pi}_{ijk}$ with volume integrals can be completely avoided by a variant of the recursion procedure based on a one step-Navier–Stokes solver iteration. The first author has successfully carried this out for diffuser flow (Narayanan *et al.* 1999).

Appendix C. Numerical computation of an empirical pressure model

In this Appendix, another pressure model is proposed for the case in which the snapshots contain pressure fields and in which no Poisson equation is to be solved. This variant is based on the observation that the omission of the quadratic terms in a_i, $i = 1, \ldots, N$, in the pressure-force representation (2.19) leads to negligible error. It should be noted here that $a_0\, a_0 = 1$ is a constant and $a_0 a_i = a_i$, $i = 1, \ldots, N$, a linear term.

Let $\boldsymbol{u}^m$, $m = 1, 2, \ldots, M$, represent the velocity snapshots, p^m the corresponding pressure fields, and $a_i^m = (\boldsymbol{u}^m - \boldsymbol{u}_0, \boldsymbol{u}_i)_\Omega$ the corresponding expansion coefficients. The ansatz of the empirical approach is given by

$$(\boldsymbol{u}_i, -\nabla p)_\Omega = \sum_{j=0}^{N} l^{\pi}_{ij} a_j. \tag{C 1}$$

Substituting p^m and a_j^m for all snapshots $m = 1, \ldots, M$ in (C 1) leads to a linear system for the $N+1$ coefficients l^{π}_{ij}. Typically $M \gg N$ and the system is overdetermined. Linear regression yields the coefficients. Alternatively, (2.17) can be employed to derive analytical formulae for l^{π}_{ij} upon multiplication of (C 1) with a_i. These formulae are exactly valid if the snapshots for the fit have also been employed for the construction of the Karhunen–Loève modes.

Galerkin systems with empirical and analytical pressure models have numerically been found to have comparable accuracies for the flows presented. The linear dependency agrees with a local linear stability analysis. For laminar and transitional absolutely unstable cylinder wake flows, the approximation for the empirical variant is still acceptable for an $<1\%$ amplitude error. It should be noted that the fluctuation level behind a cylinder wake is about one order of magnitude larger than in the shear-layer configurations presented.

In a recent study of wake flows, Galletti *et al.* (2004) use the same ansatz (C 1) for the pressure term. In that study the coefficients l^{π}_{ij} are determined from an optimization problem which minimizes the error between the Galerkin solution and the Navier–Stokes simulation. The present empirical approach minimizes the error between the pressure term in primitive variables and in the Galerkin model representation. By construction, the term of Galletti *et al.* (2004) is more accurate in the short term whereas the present term is more forgiving of long-term phase errors.

Appendix D. Transient dynamics

In this brief Appendix, the transient dynamics of the shear layer and the low-dimensional modelling process is discussed. This outline parallels an investigation of a transient cylinder wake by Noack *et al.* (2003).

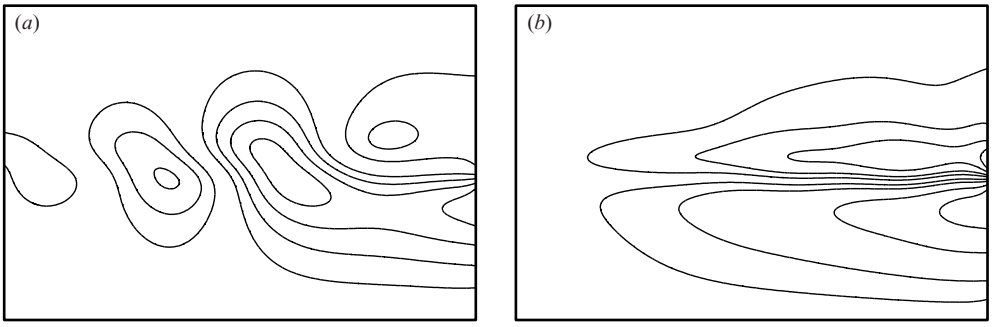

FIGURE 13. Simulation of a transient shear layer. (*a*) Instantaneous fluctuation streamlines at time $t/T = 11/8$, where T is the period. (*b*) Shift mode which is added to the Galerkin approximation (2.14) as fifth mode and describes the difference between the initial parallel flow and the averaged post-transient flow, modulo the orthonormal correction with respect to the first Karhunen–Loève modes.

The parallel flow with tanh profile (2.3) is chosen as initial condition. This velocity field is a steady solution of the Navier–Stokes equation for vanishing inflow perturbations and $Re \to \infty$. At the Reynolds number considered here, (2.3) is still a good approximation of the steady solution, since the diffusive self-similar growth of a steady shear layer (cf. Noack *et al.* 2002) is much smaller than the growth of the averaged unsteady flow.† The initial condition is incorporated in the Galerkin approximation (2.14) as an additional shift mode $\boldsymbol{u}_\Delta$ (see figure 13*b*) – in complete analogy to the wake model of Noack *et al.* (2003). This mode describes the effect of the Reynolds stress on the mean flow.

The oscillation of the purely convectively unstable shear layer is introduced as inflow condition – in contrast to the oscillatory wake which is self-excited due to an absolute instability. The Kelvin–Helmholtz vortices are generated at the inflow and grow as they convect downstream. The first vortex created after the start of the simulation generates, by the Bio-Savart law, a 'downwash' because of the missing contributions from downstream vortices (see figure 13*a*). This truncation effect is apparently not described in the Galerkin approximation based on the periodic flow – even if the shift mode is included. This transient phenomenon leads to a large unresolved residual fluctuation in the Galerkin approximation (see figure 14*a*). The transient time is about 3 periods and ends when the first vortex has crossed the outflow boundary. The expansion coefficients (see figure 14*b*) show the growth of the oscillation and the quick convergence of the shift-mode amplitude a_Δ to its asymptotic value 0.

The evolution of the expansion coefficients is described by two Galerkin models: the representation of § 3 (see figure 15*a*) and a description enriched by the shift mode (figure 15*b*). Both models include the analytical pressure-term representation. The Galerkin systems qualitatively reproduce the transient dynamics, in particular the faster convergence of the shift mode to its asymptotic value compared to the saturation of the oscillation (see figure 15*b*). However, the time scales for convergence are two orders of magnitudes too large. The reason is related to the large residuum of the Galerkin approximation. The 5-dimensional Galerkin approximation adequately

† The self-similar solution is not adopted as initial condition since it does not exactly satisfy the Dirichlet condition of the Navier–Stokes simulation.

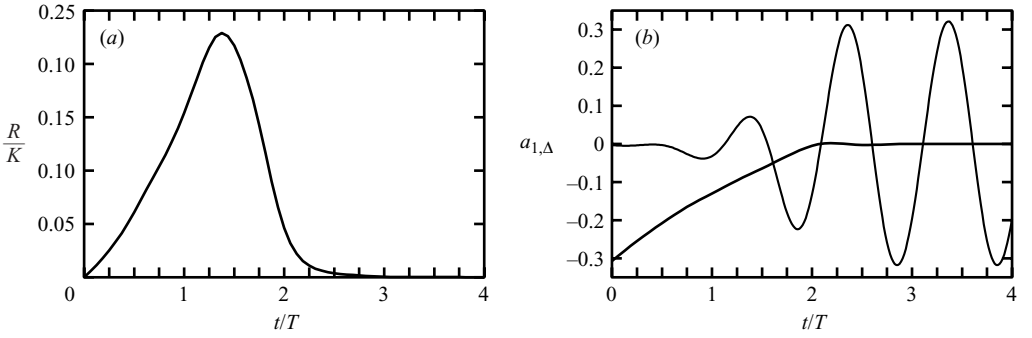

FIGURE 14. Galerkin approximation for the transient simulation of figure 13. (*a*) Energy residuum R of the 5-dimensional Galerkin approximation, normalized with the averaged post-transient fluctuation energy $\mathscr{K}$, versus time non-dimensionalized with the period T. (*b*) Temporal evolution of the expansion coefficients a_1 (thin curve) and a_Δ (thick curve). The snapshot of figure 13 has been taken at the instant of maximum residuum.

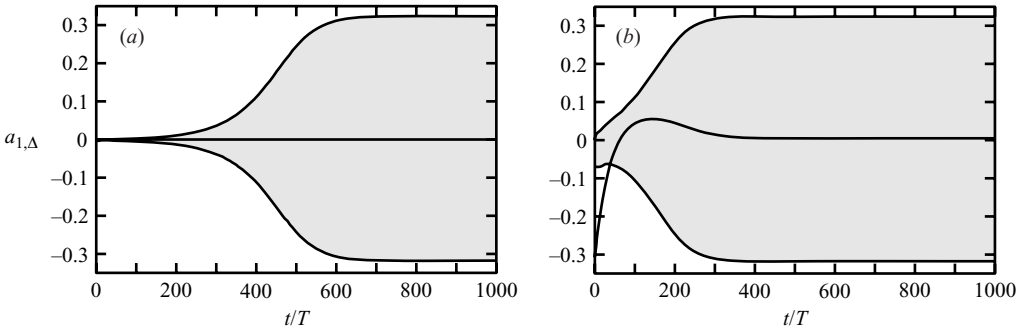

FIGURE 15. Transient solution of the Galerkin model. (*a*) 4-dimensional Galerkin approximation of § 3. (*b*) Same representation enhanced by the shift mode of figure 13. The initial conditions of the Galerkin solutions correspond to the transient flow of figure 13. The shaded zone shows the envelope of a_1. Solid curve: Shift-mode amplitude a_Δ vanishing identically by construction (*a*) or converges to 0 (*b*).

describes travelling waves, even with varying amplitudes, but individual convective vortices are not well-represented. In order to improve the transient behaviour of the model, many more modes are necessary. These may be extracted from a transient simulation following the recipes of Jørgensen *et al.* (2003). Alternative approaches based on enriched snapshot ensembles are described by Ma & Karniadakis (2002) and Bergmann *et al.* (2004)

The shift mode is seen to have an accelerating effect on the transient dynamics compared to the Galerkin model of § 3 (see figure 15). However, the effect is much weaker than in the wake model of Noack *et al.* (2003), since the production of wake vortices is more strongly dependent on the base flow which is modified by the shift mode.

REFERENCES

ASHURST, W. & MEIBURG, E. 1988 Three-dimensional shear layers via vortex dynamics. *J. Fluid Mech.* **189**, 87–116.

AUBRY, N., HOLMES, P., LUMLEY, J. & STONE, E. 1988 The dynamics of coherent structures in the wall region of a turbulent boundary layer. *J. Fluid Mech.* **192**, 115–173.

Bergmann, M., Cordier, L. & Brancher, J.-P. 2004 Optimal rotary control of the cylinder wake using POD reduced order model. *AIAA Paper* 2004-2323.

Bertolotti, F., Herbert, T. & Spalart, P. 1992 Linear and nonlinear stability of the Blasius boundary layer. *J. Fluid Mech.* **242**, 441–474.

Blossey, P. & Lumley, J. 1998 Control of turbulence. *Annu. Rev. Fluid Mech.* **30**, 311–327.

Coats, C. 1997 Coherent structures in combustion. *Prog. Energy Combust. Sci.* **22**, 427–509.

Coller, B., Noack, B. R., Narayanan, S., Banaszuk, A. & Khibnik, A. 2000 Reduced-basis model for active separation control in a planar diffuser flow. *AIAA Paper* 2000-2563.

Comte, P., Silvestrini, J. H. & Bégou, P. 1998 Streamwise vortices in large-eddy simulations of mixing layer. *Eur. J. Mech.* B **17**, 615–637.

Cordier, L., Tenaud, C. & Delville, J. 1998 Low-dimensional model of a plane turbulent mixing layer. In *Proc. 13th Australasian Fluid Mechanics Conference, Monash University, Melbourne, Australia, Dec. 13–18, 1998* (ed. M. C. Thompson & K. Hourigan). Monash University.

Deane, A., Kevrekidis, I., Karniadakis, G. & Orszag, S. 1991 Low-dimensional models for complex geometry flows: Application to grooved channels and circular cylinders. *Phys. Fluids* A **3**, 2337–2354.

Delville, J., Ukeiley, L., Cordier, L., Bonnet, J. & Glauser, M. 1999 Examination of large-scale structures in a turbulent plane mixing layer. Part 1. Proper orthogonal decomposition. *J. Fluid Mech.* **391**, 91–122.

Gad-el-Hak, M. 1996 Modern developments in flow control. *Appl. Mech. Rev.* **49**, 365–379.

Gad-el-Hak, M. 2000 *Flow Control: Passive, Active and Reactive Flow Management*. Cambridge University Press.

Galletti, G., Bruneau, C. H., Zannetti, L. & Iollo, A. 2004 Low-order modelling of laminar flow regimes past a confined square cylinder. *J. Fluid Mech.* **503**, 161–170.

Gerhard, J., Pastoor, M., King, R., Noack, B. R., Dillmann, A., Morzyński, M. & Tadmor, G. 2003 Model-based control of vortex shedding using low-dimensional Galerkin models. *AIAA Paper* 2003-4262.

Holmes, P., Lumley, J. & Berkooz, G. 1998 *Turbulence, Coherent Structures, Dynamical Systems and Symmetry*. Cambridge University Press.

Jørgensen, B. H., Sørensen, J. N. & Brøns, M. 2003 Low-dimensional modeling of a driven cavity flow with two free parameters. *Theoret. Comput. Fluid Dyn.* **16**, 299–317.

Kaltenbach, H.-J., Mittal, F., Lund, T. & Moin, P. 1999 Study of flow in a planar asymmetric diffuser using large-eddy simulation. *J. Fluid Mech.* **390**, 151–185.

Lorenz, E. 1963 Deterministic nonperiodic flow. *J. Atmos. Sci.* **20**, 130–141.

Ma, X. & Karniadakis, G. 2002 A low-dimensional model for simulating three-dimensional cylinder flow. *J. Fluid Mech.* **458**, 181–190.

Michalke, A. 1964 On the inviscid instability of the hyperbolic-tangent velocity profile. *J. Fluid Mech.* **19**, 543–556.

Moehlis, J., Smith, T., Holmes, P. & Faisst, H. 2002 Models for turbulent plane Couette flow using the proper orthogonal decomposition. *Phys. Fluids* **14**, 2493–2507.

Monin, A. & Yaglom, A. 1971 *Statistical Fluid Mechanics I*. The MIT Press.

Monkewitz, P. A. & Huerre, P. 1982 Influence of the velocity ratio on the spatial instability of mixing layers. *Phys. Fluids* **25**, 1137–1143.

Narayanan, S., Noack, B. R., Banaszuk, A. & Khibnik, A. 1999 Dynamic separation control in 2D diffuser. *Tech. Rep.* 1.910.9901-4.1. United Technologies Research Center, E. Hartford, CT, USA.

Narayanan, S., Noack, B. R. & Meiburg, E. 2002 Reduced-order dynamical modeling of sound generation from a jet. *AIAA Paper* 2002-0073.

Noack, B. R., Afanasiev, K., Morzyński, M. & Thiele, F. 2003 A hierarchy of low-dimensional models for the transient and post-transient cylinder wake. *J. Fluid Mech.* **497**, 335–363.

Noack, B. R. & Eckelmann, H. 1994 A low-dimensional Galerkin method for the three-dimensional flow around a circular cylinder. *Phys. Fluids* **6**, 124–143.

Noack, B. R., Mezić, I., Tadmor, G. & Banaszuk, A. 2004*a* Optimal mixing in recirculation zones. *Phys. Fluids* **16**, 867–888.

Noack, B. R., Papas, P. & Monkewitz, P. A. 2002 Low-dimensional Galerkin model of a laminar shear-layer. *Tech. Rep.* 2002-01. Laboratoire de Mecanique des Fluides, Departement de Genie Mecanique, Ecole Polytechnique Fédérale de Lausanne, Switzerland.

Noack, B. R., Pelivan, P., Tadmor, G. Morzyński, M. & Comte, P. 2004*b* Robust low-dimensional Galerkin models of natural and actuated flows. In *Proc. Fourth Aeroacoustics Workshop, RWTH Aachen, February 26–27, 2004* (ed. W. Schröder & P. Tröltzsch). Institut für Akustik und Sprachkommunikation, Technical University of Dresden.

Papas, P., Monkewitz, P. A. & Tomboulides, A. G. 1999 New instability modes of a diffusion flame near extinction. *Phys. Fluids* **11**, 2818–20.

Papas, P., Rais, R., Monkewitz, P. A. & Tomboulides, A. G. 2003 Instabilities of diffusion flames near extinction. *Combustion Theory and Modelling* **7**, 603–633.

Pastoor, M., King, R., Noack, B. R. & Dillmann, A. & Tadmor, G. 2003 Model-based coherent-structure control of turbulent shear flows using low-dimensional vortex models. *AIAA Paper* 2003-4261.

Rajaae, M., Karlsson, S. K. F. & Sirovich, L. 1994 Low-dimensional description of free-shear-flow coherent structures and their dynamical behaviour. *J. Fluid Mech.* **258**, 1–29.

Rediniotis, O., Ko, J. & Kurdila, A. 2002 Reduced order nonlinear Navier-Stokes models for synthetic jets. *Trans. ASME: J. Fluids Engng* **124**, 433–443.

Rempfer, D. 1991 Kohärente Strukturen und Chaos beim laminar-turbulenten Grenzschichtumschlag (transl.: Coherent structures and chaos of the laminar-turbulent boundary-layer transition). PhD thesis, Fakultät Verfahrenstechnik der Universität Stuttgart (part of this work has been published in Rempfer & Fazle. *J. Fluid Mech.* **260** (1994), 351–375 and **275** (1994), 257–283).

Rempfer, D. 2003 Low-dimensional modeling and numerical simulation of transition in simple shear flow. *Annu. Rev. Fluid Mech.* **35**, 229–265.

Rogers, D. & Marble, F. 1954 A new mechanism for high-frequency oscillations in ramjet combustors and afterburners. *Jet Propul.* **20**, 254–262.

Rosenhead, L. 1930 The spread of vorticity in the wake behind a cylinder. *Proc. R. Soc. Lond.* A **127**, 590–612.

Sirovich, L. 1987 Turbulence and the dynamics of coherent structures, Part I: Coherent structures. *Q. Appl. Maths* **XLV**, 561–571.

Tadmor, G. & Banaszuk, A. 2002 Observer based control of vortex motion in a combuster recirculation region. In *Proc. Nonlinear Control Systems 2001* (ed. A. Kurzhanski & A. Fradkov), pp. 1315–1318. Elsevier.

Townsend, A. 1956 *The Structure of Turbulent Shear Flow*. Cambridge University Press.

Ukeiley, L., Cordier, L., Manceau, R., Delville, J., Bonnet, J. & Glauser, M. 2001 Examination of large-scale structures in a turbulent plane mixing layer. Part 2. Dynamical systems model. *J. Fluid Mech.* **441**, 61–108.

Wee, D., Park, S., Miake-Lye, R., Annaswamy, A. & Ghoniem, A. 2002 Reduced-order modeling of reacting shear layer. *AIAA Paper* 2002-0478.